

Transformation between meron and skyrmion topological spin textures in a chiral magnet

X. Z. Yu^{1*}, W. Koshibae¹, Y. Tokunaga², K. Shibata¹, Y. Taguchi¹, N. Nagaosa^{1,3} & Y. Tokura^{1,3}

Crystal lattices with tetragonal or hexagonal structure often exhibit structural transitions in response to external stimuli¹. Similar behaviour is anticipated for the lattice forms of topological spin textures, such as lattices composed of merons and antimerons or skyrmions and antiskyrmions (types of vortex related to the distribution of electron spins in a magnetic field), but has yet to be verified experimentally^{2,3}. Here we report real-space observations of spin textures in a thin plate of the chiral-lattice magnet $\text{Co}_8\text{Zn}_9\text{Mn}_3$, which exhibits in-plane magnetic anisotropy. The observations demonstrate the emergence of a two-dimensional square lattice of merons and antimerons from a helical state, and its transformation into a hexagonal lattice of skyrmions in the presence of a magnetic field at room temperature. Sequential observations with decreasing temperature reveal that the topologically protected skyrmions remain robust to changes in temperature, whereas the square lattice of merons and antimerons relaxes to non-topological in-plane spin helices, highlighting the different topological stabilities of merons, antimerons and skyrmions. Our results demonstrate the rich variety of topological spin textures and their lattice forms, and should stimulate further investigation of emergent electromagnetic properties.

Periodic atomic arrays form crystals that can have body-centred tetragonal structures or hexagonal close-packed structures¹. These structural types are also observed in topological matter, such as in the square lattice of magnetic flux in superconductors⁴ and in the hexagonal lattice of magnetic skyrmions in chiral-lattice magnets^{5–7}. (Skyrmions are topological spin textures with topological number

$$N = \frac{1}{4\pi} \int \mathbf{n} \cdot \left(\frac{\partial \mathbf{n}}{\partial x} \times \frac{\partial \mathbf{n}}{\partial y} \right) dx dy$$

where $\mathbf{n} = \mathbf{M}/|\mathbf{M}|$ and \mathbf{M} is the magnetic moment.) The structural transition between square and hexagonal lattices has been theoretically predicted² to occur in two-dimensional chiral-lattice magnets with tuning of the material parameters, such as magnetic anisotropy. Controlling the lattice form of topological objects is important to be able to use their collective dynamics in real materials³.

We study nanometre-scale topological spin textures, such as merons (vortex-like spin textures with $N = -1/2$), antimerons and skyrmions, to confirm experimentally the transformation between the square and hexagonal lattices. Skyrmions with $N = -1$ have been discovered in chiral and polar magnets and at ferromagnetic interfaces, in which the antisymmetric spin exchange interaction arises from relativistic spin–orbit coupling (Dzyaloshinskii–Moriya interaction)^{2,3,5–15}. In a skyrmion, whole magnetic moments swirl from the south pole at the core to the north pole at the perimeter, encompassing a sphere. The hexagonal skyrmion lattice is thermodynamically stabilized by the hybridization of three helices lying within the plane perpendicular to the magnetic field in chiral-lattice magnets^{5–7}.

Merons ($N = -1/2$) and antimerons ($N = +1/2$) are topologically distinct from skyrmions ($N = -1$) and antiskyrmions¹⁶ ($N = +1$);

in merons and antimerons, the magnetic moments in the core region point upwards or downwards, and those near the perimeter align in-plane, producing degrees of freedom for magnetic helicity and polarity⁷ (Fig. 1a–d). The topological number N of skyrmions and antiskyrmions is determined by the product of the vorticity (the rotation direction of the in-plane component of the magnetic moments) and the direction of the magnetic moment in the core⁷. We classify merons and antimerons according to the sign of N .

Merons, antimerons and skyrmions, and the structural transitions of their lattices, are expected to be realized under the condition of increased magnetic anisotropy, which is also crucial for controlling topological spin textures in chiral-lattice systems². Several theoretical studies have asserted that in-plane magnetic anisotropy energetically stabilizes the square lattice of merons and antimerons, rather than the hexagonal skyrmion lattice that otherwise forms owing to the competition between the Dzyaloshinskii–Moriya and ferromagnetic interactions^{2,3,17,18}. However, merons and antimerons, and their lattice forms, have not yet been observed experimentally, although micrometre-scale artificial merons with random vorticities have been reported in permalloys^{19–22}.

Here, we report the experimental observation of merons and antimerons, and the transformation from the square (anti)meron lattice to the hexagonal skyrmion lattice. We present direct real-space imaging of topological spin textures in a thin plate of the chiral-lattice magnet $\text{Co}_8\text{Zn}_9\text{Mn}_3$, which exhibits the Dzyaloshinskii–Moriya interaction and has a high (above room temperature) transition temperature to the helical state (T_C)⁸. We also reveal the different topological stability for merons and skyrmions.

In Fig. 1e we show a schematic of the square (anti)meron lattice, which is described by a ‘double \mathbf{q} ’ structure with orthogonal \mathbf{q} vectors, where \mathbf{q} is the wavevector of in-plane helices. In Fig. 1f we present the magnetization textures observed in a (001) thin plate of $\text{Co}_8\text{Zn}_9\text{Mn}_3$ at 295 K by means of Lorentz transmission electron microscopy (TEM) with a normal magnetic field of 20 mT after a 10-mT field cooling. The white arrows and colours in Fig. 1f denote the magnitude and the direction of the in-plane magnetization, whereas the dark colour indicates the out-of-plane magnetizations²³. A comparison between Fig. 1e and Fig. 1f indicates that the experimentally observed spin texture coincides with the square (anti)meron lattice. The square (anti)meron lattice consists of periodic arrays of alternating convergence and divergence of magnetization, as theoretically predicted. Figure 1f clearly demonstrates these periodic arrays. Figure 1f also indicates that the maximum in-plane magnetization is observed at the periphery of merons and antimerons, whereas the minimum (almost zero) is at the core. In comparison with the theoretical prediction of square (anti)meron lattices (Fig. 1e), the out-of-plane magnetization at the cores of adjacent merons and antimerons with a vorticity of $+1$ are plausibly antiparallel, although the Lorentz TEM is unable to confirm the direction of the out-of-plane magnetization parallel to the incident electron beam. On the other hand, the merons with a vorticity of -1 prefer the upwards-pointing core magnetizations parallel to the external field

¹RIKEN Center for Emergent Matter Science (CEMS), Wako, Japan. ²Department of Advanced Materials Science, University of Tokyo, Kashiwa, Japan. ³Department of Applied Physics, University of Tokyo, Tokyo, Japan. *e-mail: yu_x@riken.jp

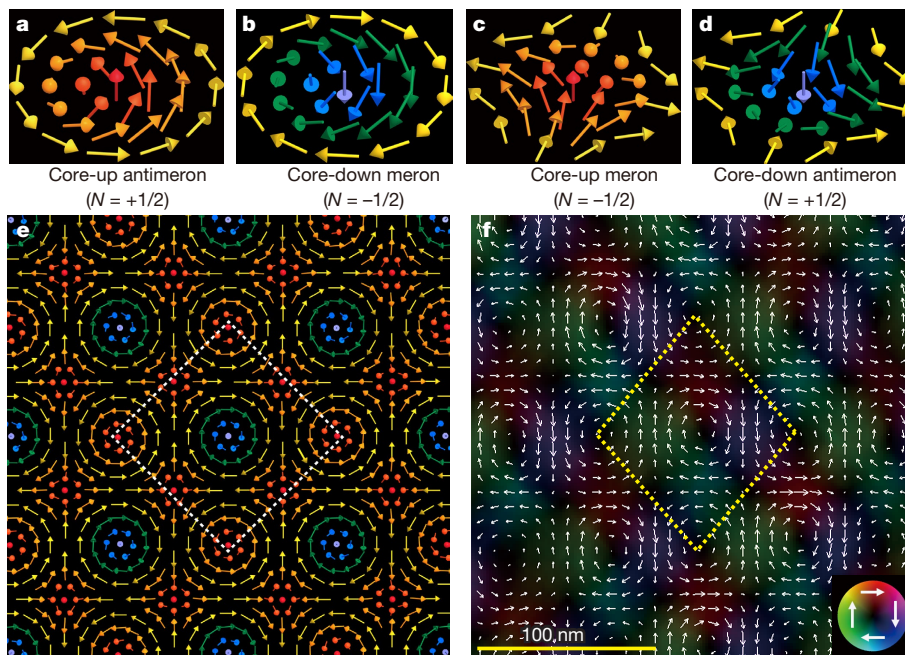


Fig. 1 | Real-space observations of a square lattice of merons and antimerons in a thin plate of the chiral-lattice magnet $\text{Co}_8\text{Zn}_9\text{Mn}_3$. **a–d**, Schematics of the magnetization textures of a core-up antimeron (**a**) and a core-down meron (**b**), each with a vorticity of $+1$, and a core-up meron (**c**) and a core-down antimeron (**d**), each with a vorticity of -1 . Coloured arrows indicate directions of the magnetic moments. **e**, Theoretically predicted square (anti)meron lattice. **f**, Real-space magnetization textures of the square (anti)meron lattice, observed by

direction, resulting in an energetically stabilized square (anti)meron lattice in the thin plate. An in situ Lorentz TEM video (Supplementary Video 1) demonstrates the formation process of the square (anti)meron lattice. Composed of merons and antimerons, it can be viewed as the hybridization of two in-plane helices; this is in contrast to the formation of the hexagonal skyrmion lattice with the hybridization of three helices under a higher field, in which no antiskyrmions appears. In comparison to the ideal case (Fig. 1e), the square (anti)meron lattice observed in a (001) $\text{Co}_8\text{Zn}_9\text{Mn}_3$ thin plate seems to elongate in the vertical direction, possibly because of the effect of strain on the spin textures in the thin plate²⁴.

We obtained experimental evidence for the transformation of the square (anti)meron lattice into the hexagonal skyrmion lattice at 295 K by finely varying the normal field. In Fig. 2a, b we show magnified snapshots from Supplementary Video 1 under 20 mT and 50 mT. The image for a higher magnetic field (60 mT; Fig. 2c) was taken separately, as a still image (see details in Methods and Extended Data Fig. 1c for the experimental procedure). Upon increasing the bias field, the real-space images and the related fast Fourier transforms (Fig. 2a–c, insets) reveal a transformation from a square lattice (Fig. 2a) to a hexagonal lattice (Fig. 2c) via a deformed square lattice (Fig. 2b) of the spin textures. The continuous deformation of the spin textures appears concurrently in the lattice transformation process.

In Fig. 2d–f we show enlarged magnetization textures in the boxed areas of Fig. 2a–c. In Fig. 2d, alternating core-down merons and core-up antimerons, accompanied by core-up merons, appear to form a square (anti)meron lattice. When the field is increased to 50 mT (Fig. 2e), the in-plane components (along the dashed lines) become small, indicating that the magnetization tends to point up. This means that the core-up merons turn into ferromagnetic regions between skyrmions, which form the deformed square lattice. Further increasing the field to 60 mT, the core-up antimerons change completely to out-of-plane field-magnetized domains, and the hexagonal skyrmion lattice is stabilized (Fig. 2f). The observed magnetization textures for square (anti)meron and hexagonal skyrmion lattices agree well with micromagnetic

using Lorentz TEM under a 20-mT field applied normally to a (001) thin plate of $\text{Co}_8\text{Zn}_9\text{Mn}_3$ after 10-mT field cooling from 340 K (above the helical-ordering transition temperature $T_C \approx 325 \text{ K}$ ³⁰). The thickness of the thin plate is approximately 100 nm; the width and length are approximately 10 μm and 50 μm , respectively. The arrows and colour scale indicate the direction and magnitude of the in-plane magnetization; black indicates out-of-plane magnetization. The dashed lines in **e** and **f** define a unit cell of the square (anti)meron lattice.

simulations (Extended Data Fig. 2). As an important feature of the transition between the lattices, the total topological number does not change during the continuous deformation of the spin texture.

In Fig. 2g–i we show a schematic of the transformation that we observe. In the square (anti)meron lattice (Fig. 2g), the total topological number N_{total} in the unit (bounded by dashed lines) composed of one core-down meron ($N = -1/2$), four quarters of core-up antimerons ($N = +1/2$) and four halves of core-up merons ($N = -1/2$) is $N_{\text{total}} = -1/2 + (+1/2) \times (1/4) \times 4 + (-1/2) \times (1/2) \times 4 = -1$. As the bias field increases, the square (anti)meron lattice deforms continuously to the square skyrmion lattice, accompanied by the transformation of core-up merons and antimerons to field-magnetized moments surrounding a core-down skyrmion (Fig. 2h). The topological number for the unit (bounded by dashed lines) composed of one skyrmion is -1 . Further increasing the bias field possibly induces a transformation from the square to the hexagonal skyrmion lattice, while keeping the topological number of -1 in the unit (bounded by dashed lines; Fig. 2i). This interpretation is plausible for the transformation observed here, indicating the topological invariance of spin textures.

To examine the stability of the meron and the antimeron in the thin plate, we created a square (anti)meron lattice at 295 K following the procedure described above and then cooled the thin plate to temperatures far below T_C while keeping the bias field of 20 mT. In Fig. 3a–d we show the Lorentz TEM images observed at several temperatures in this procedure. The same experimental protocol was used to check the stability of the hexagonal skyrmion lattice field-cooled at 60 mT. In Fig. 3e–h we show the skyrmion lattice observed at various temperatures during the field cooling. At 295 K, we observe the square (anti)meron lattice at 20 mT (Fig. 3a) and the hexagonal skyrmion lattice at 60 mT (Fig. 3e). With the decrease in temperature, the square (anti)meron lattice becomes deformed and finally collapses to almost in-plane helices at about 120 K; at this temperature, the non-topological helical and conical phases are dominant as the thermodynamically stable states in the thin plate under zero and 10-mT field cooling (Extended Data Fig. 1). In contrast to the destabilization of the square (anti)meron lattice at lower

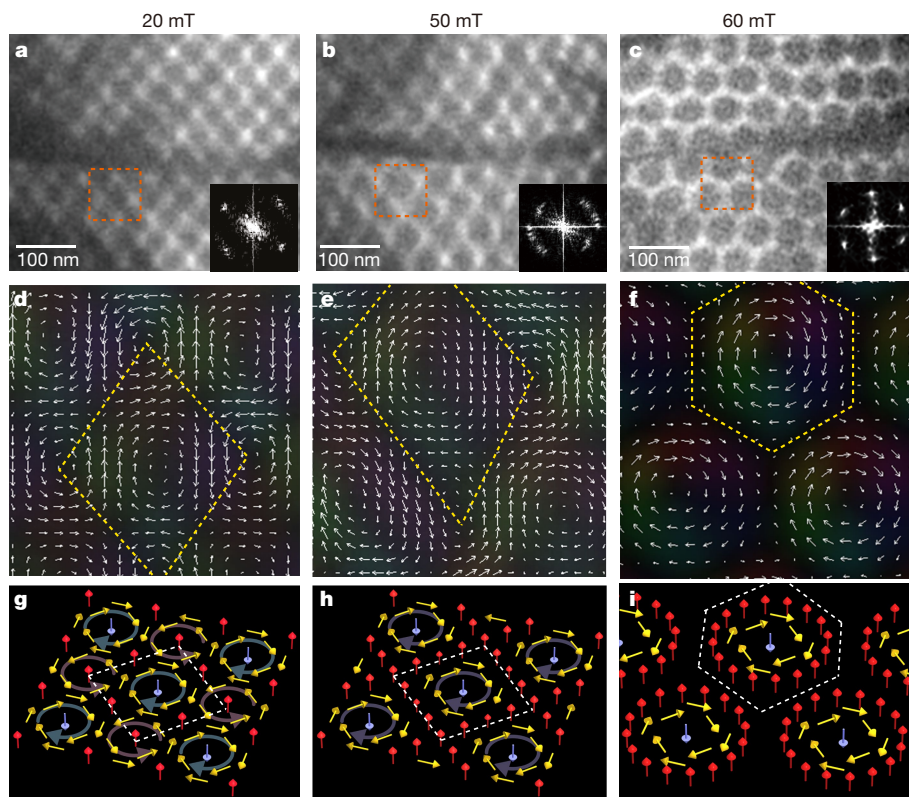


Fig. 2 | Magnetically induced transformation of a square (anti)meron lattice to a hexagonal skyrmion lattice via a deformed skyrmion lattice in the (001) plate of $\text{Co}_8\text{Zn}_9\text{Mn}_3$ at 295 K. a–c, Over-focused Lorentz TEM images and related fast Fourier transforms (insets) observed with increasing field, while keeping the temperature at 295 K after 10-mT field cooling (the experimental procedure is denoted by a black arrow in the phase diagram in Extended Data Fig. 1c). The Lorentz TEM image in c was obtained by tilting the thin plate slightly (about 2°) to remove the diffractive contrast and hence increase the intensity of the magnetic signal. The bias field affects the condition of the electron beam slightly because the field is below 100 mT for our observations. d–f, Magnetization textures obtained by analysing the boxed regions of the Lorentz TEM images in a–c, respectively, using the software Qpt²³, which is based on the transport-of-intensity equation (see Methods). Colours and arrows as in Fig. 1f. g–i, Schematics of the magnetization textures for the square (anti)meron lattice (g), the deformed square skyrmion lattice (h) and the hexagonal skyrmion lattice (i). The dashed regions in d–i indicate the units of the spin textures, each with a topological number of $N = -1$.

temperatures, the hexagonal skyrmion lattice survives, and no topological phase transition occurs with decreasing temperature, although the shape of the individual skyrmion becomes deformed, possibly owing to the effect of anisotropic strain. The magnetization textures of the boxed regions in Fig. 3d (20 mT) and Fig. 3h (60 mT) at 120 K are shown in

Fig. 3i and Fig. 3j, respectively, with the colour wheel indicating the in-plane magnetization direction. These images confirm that only a few core-up antimerons remain in the matrix of in-plane helices with orthogonal q vectors at 20 mT and 120 K. By contrast, in the case of field cooling at 60 mT, the hexagonal deformed-skyrmion lattice exists

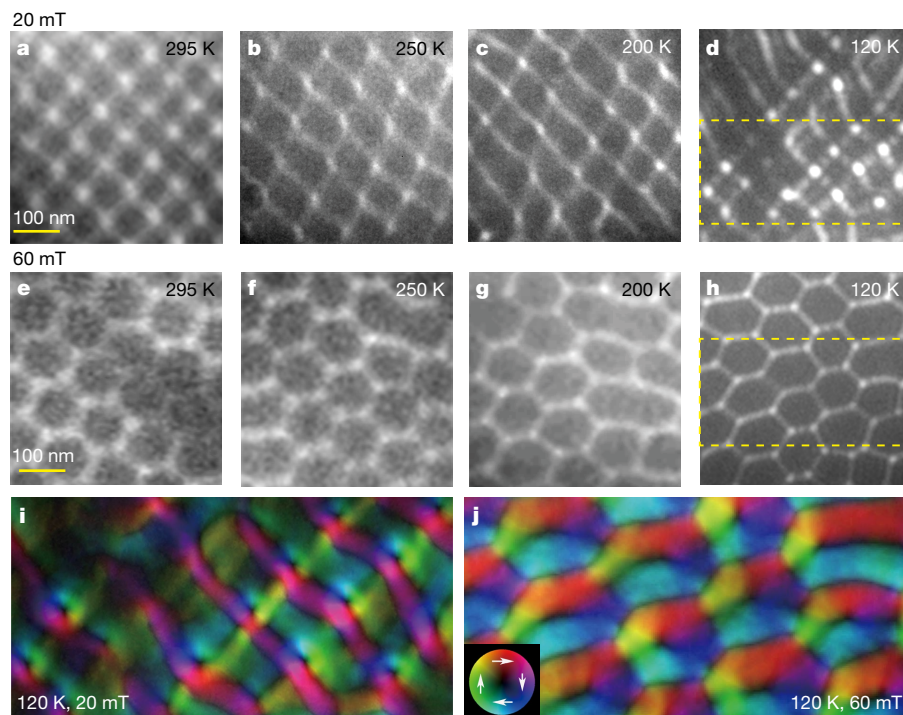


Fig. 3 | Stability of the square (anti)meron and hexagonal skyrmion lattices in the (001) plate of $\text{Co}_8\text{Zn}_9\text{Mn}_3$. a–h, Over-focused Lorentz TEM images of the square (anti)meron (a–d) and hexagonal skyrmion (e–h) lattices observed with decreasing temperature at a magnetic field of 20 mT and 60 mT, respectively (experimental procedures are denoted by

red dashed arrows in the phase diagram in Extended Data Fig. 3b). i, j, Magnetization textures for the boxed regions in d and h, respectively, deduced by analysing Lorentz TEM images with the transport-of-intensity equation. The colour wheel in the inset of j indicates the in-plane magnetization direction.

robustly at the same temperature (see also the temperature–field phase diagram in Extended Data Fig. 3). The result for the field cooling at 60 mT is in accord with previous experimental studies on topologically protected skyrmions in chiral-lattice magnets^{25–29}.

With in-plane anisotropy (Methods, Extended Data Figs. 1, 5, 6), it is natural to anticipate the formation of merons and antimerons because of the consistent vorticities between the neighbouring spin textures³. In addition, the region surrounded by the two merons and two antimerons has a vorticity of -1 and the upwards-pointing magnetic field generates core-up moments, which results in the meron (Fig. 2g). This is why the square (anti)meron lattice forms at weak magnetic fields. Although metastability is also discerned for the square (anti)meron lattice beyond thermal equilibrium (compare Extended Data Figs. 1c and 3b), the (anti)meron lattice is easier to deform to a helix than is the skyrmion lattice, because the total magnetization and each topological number are smaller, so the potential barrier to change the topological number is expected to be smaller. In this sense, we consider the square (anti)meron lattice to be located between a helix and a skyrmion lattice.

Online content

Any methods, additional references, Nature Research reporting summaries, source data, statements of data availability and associated accession codes are available at <https://doi.org/10.1038/s41586-018-0745-3>.

Received: 12 July 2018; Accepted: 11 October 2018;

Published online 5 December 2018.

- Kittel, C. *Introduction to Solid State Physics* Ch. 1 (John Wiley & Sons, New York, (2005).
- Lin, S. Z., Saxena, A. & Batista, C. D. Skyrmion fractionalization and merons in chiral magnets with easy-plane anisotropy. *Phys. Rev. B* **91**, 224407 (2015).
- Yi, S. D., Onoda, S., Nagaosa, N. & Han, J. H. Skyrmions and anomalous Hall effect in a Dzyaloshinskii–Moriya spiral magnet. *Phys. Rev. B* **80**, 054416 (2009).
- Berdiyrov, G. R., Milošević, M. V. & Peeters, F. M. Vortex configurations and critical parameters in superconducting thin films containing antidote arrays: nonlinear Ginzburg–Landau theory. *Phys. Rev. B* **74**, 174512 (2006).
- Mühlbauer, S. et al. Skyrmion lattice in a chiral magnet. *Science* **323**, 915–919 (2009).
- Yu, X. Z. et al. Real-space observation of a two-dimensional skyrmion crystal. *Nature* **465**, 901–904 (2010).
- Nagaosa, N. & Tokura, Y. Topological properties and dynamics of magnetic skyrmions. *Nat. Nanotechnol.* **8**, 899–911 (2013).
- Tokunaga, Y. et al. A new class chiral materials hosting magnetic skyrmions beyond room temperature. *Nat. Commun.* **6**, 7638 (2015).
- Heinze, S. et al. Spontaneous atomic-scale magnetic skyrmion lattice in two dimensions. *Nat. Phys.* **7**, 713–718 (2011).
- Kézsmárki, I. et al. Néel-type skyrmion lattice with confined orientation in the polar magnetic semiconductor GaV_4S_8 . *Nat. Mater.* **14**, 1116–1122 (2015).
- Li, W. et al. Emergence of skyrmions from rich parent phases in the molybdenum nitrides. *Phys. Rev. B* **93**, 060409(R) (2016).
- Woo, S. et al. Observation of room-temperature magnetic skyrmions and their current-driven dynamics in ultrathin metallic ferromagnets. *Nat. Mater.* **15**, 501–506 (2016).
- Jiang, W. et al. Blowing magnetic skyrmion bubbles. *Science* **349**, 283–286 (2015).
- Sampaio, J., Cros, V., Rohart, S., Thiaville, A. & Fert, A. Nucleation, stability and current-induced motion of isolated magnetic skyrmions in nanostructures. *Nat. Nanotechnol.* **8**, 839–844 (2013).
- Zheng, F. S. et al. Experimental observation of chiral magnetic bobbles in B20-type FeGe. *Nat. Nanotechnol.* **13**, 451–455 (2018).
- Nayak, A. K. et al. Magnetic antiskyrmions above room temperature in tetragonal Heusler materials. *Nature* **548**, 561–566 (2017).
- Ozawa, R. et al. Vortex crystals with chiral stripes in itinerant magnets. *J. Phys. Soc. Jpn* **85**, 103703 (2016).
- Vousden, M. et al. Skyrmions in thin films with easy-plane magnetocrystalline anisotropy. *Appl. Phys. Lett.* **108**, 132406 (2016).
- Shinjo, T., Okuno, T., Hassdorf, R., Shigeko, K. & Ono, T. Magnetic vortex core observation in circular dots of permalloy. *Science* **289**, 930–932 (2000).
- Phatak, C., Petford-Long, A. K. & Heinonen, O. Direct observation of unconventional topological spin structure in coupled magnetic discs. *Phys. Rev. Lett.* **108**, 067205 (2012).
- Wintz, S. et al. Topology and origin of effective spin meron pairs in ferromagnetic multilayer elements. *Phys. Rev. Lett.* **110**, 177201 (2013).
- Tan, A. et al. Topology of spin meron pairs in coupled Ni/Fe/Co/Cu (001) disks. *Phys. Rev. B* **94**, 014433 (2016).
- Ishizuka, K. & Allman, B. Phase measurement in electron microscopy using the transition of intensity equation. *J. Electron Microsc.* **54**, 191–197 (2005).
- Shibata, K. et al. Large anisotropic deformation of skyrmions in strained crystals. *Nat. Nanotechnol.* **10**, 589–592 (2015).
- Karube, K. et al. Robust metastable skyrmions and their triangular–square lattice structural transition in a high-temperature chiral magnet. *Nat. Mater.* **15**, 1237–1242 (2016).
- Nakajima, T. et al. Skyrmion lattice structural transition in MnSi. *Sci. Adv.* **3**, e1602562 (2017).
- Oike, H. et al. Interplay between topological and thermodynamic stability in a metastable magnetic skyrmion lattice. *Nat. Phys.* **12**, 62–66 (2016).
- Münzer, W. et al. Skyrmion lattice in the doped semiconductor $\text{Fe}_{1-x}\text{Co}_x\text{Si}$. *Phys. Rev. B* **81**, 041203(R) (2010).
- Yu, X. Z. et al. Aggregation and collapse dynamics of skyrmions in a non-equilibrium state. *Nat. Phys.* **14**, 832–836 (2018).
- Yu, X. Z. et al. Current-induced nucleation and annihilation of magnetic skyrmions at room temperature in a chiral magnet. *Adv. Mater.* **29**, 1606178 (2017).

Acknowledgements We thank M. Ishida, Á. Butykai, D. Morikawa, T.-H. Arima and M. V. Mostovoy for experimental support and discussions. N.N. was supported by JSPS KAKENHI (grant numbers JP26103006 and JP18H03676) and JST CREST (grant number JPMJCR1874), Japan.

Reviewer information Nature thanks S. Woo and the other anonymous reviewers for their contribution to the peer review of this work.

Author contributions Y. Tokura conceived the project. X.Z.Y. performed Lorentz TEM and analysed the experimental data. W.K. and N.N. performed the theoretical analyses. Y. Tokunaga and Y. Taguchi synthesized the Co-Zn-Mn alloys. K.S. simulated the Lorentz TEM images. All authors discussed the data and collaborated on the manuscript.

Competing interests The authors declare no competing interests.

Additional information

Extended data is available for this paper at <https://doi.org/10.1038/s41586-018-0745-3>.

Supplementary information is available for this paper at <https://doi.org/10.1038/s41586-018-0745-3>.

Reprints and permissions information is available at <http://www.nature.com/reprints>.

Correspondence and requests for materials should be addressed to X.Z.Y.

Publisher's note: Springer Nature remains neutral with regard to jurisdictional claims in published maps and institutional affiliations.

METHODS

Sample preparation and experimental methods. Bulk Co-Zn-Mn alloys were synthesized using procedures described elsewhere^{8,30}. The thin plates for the Lorentz TEM observations were prepared by an Ar-ion milling process after mechanical polishing of the bulk sample. Real-space observations were performed using a multifunctional TEM (JEM2800, JEOL) equipped with single-tilt heating/cooling (HC 3500) and double-tilt nitrogen cooling (Gatan 636) holders. The temperature of the thin plate was controlled between 95 K and 350 K. The magnetic configurations were obtained by Lorentz TEM observations.

Characterization of magnetization textures in a thin plate of Co₈Zn₉Mn₃. Lorentz TEM is useful for observing the in-plane magnetic configurations in thin magnets. The convergence (divergence) of the electron beam reflecting the in-plane magnetization distribution can be imaged in the defocused Lorentz TEM images as bright (dark) contrast because of the interactions between the incident electrons and the in-plane magnetic components in thin magnets. Such contrasts should reverse in under-focused and over-focused Lorentz TEM images. Therefore, an ideal screw structure that follows the direction of the in-plane wavevector can be projected as alternating bright and dark stripes with a constant period. For skyrmions that exhibit clockwise (anticlockwise) helicity, the bright (dark) dots should appear in the defocused image plane. We extracted electron-phase images and then converted them to magnetization textures to avoid blurring and artificial background noise caused by the surface roughness of the sample using the software Qpt²³, which is based on the transport-of-intensity equation:

$$\frac{2\pi}{\lambda} \frac{\partial I(x, y, z)}{\partial z} = -\nabla_{xy} \cdot [I(x, y, z) \nabla_{xy} \varphi(x, y, z)] \quad (1)$$

where λ , $I(x, y, z)$ and $\varphi(x, y, z)$ represent the wavelength, intensity and phase of the incident electron beam, respectively. The gradient of the electron-beam intensity ($\partial I(x, y, z)/\partial z$) in the under-focused and over-focused Lorentz TEM images enables us to obtain $\nabla_{xy} \varphi(x, y, z)$. The Maxwell–Ampère equation establishes a relationship between $\varphi(x, y, z)$ and the magnetization M :

$$\nabla_{xy} \varphi(x, y, z) = -\frac{e}{\hbar} (M \times n) t \quad (2)$$

where t and n are the sample thickness and unit vector perpendicular to the sample surface, respectively.

Crystal structure, magnetic structure and magnetic phase diagrams observed in a thin plate of Co₈Zn₉Mn₃ with a low-field (10 mT) cooling procedure. The Co₈Zn₉Mn₃ alloy crystallizes in a chiral cubic structure with space group $P4_132$ or $P4_332$ (Extended Data Fig. 1a, b)⁸. Extended Data Fig. 1c shows the magnetic phase diagram of the thin Co₈Zn₉Mn₃ obtained from field-increasing runs after low-field (<10 mT) cooling. The hexagonal skyrmion lattice (hex-SkL) phase (red-coloured region in Extended Data Fig. 1c) and the square lattice of merons and antimerons (sq-ML) (green-coloured region in Extended Data Fig. 1c) are thermodynamically stabilized in a narrow window near T_C . The helical structure at zero field and the conical structure under a finite bias field are dominant at lower temperatures. Extended Data Fig. 1d demonstrates the striped domains of in-plane helices at a lower temperature (for example, 95 K); when the temperature is increased to 295 K (Extended Data Fig. 1e), the striped domains turn into multi-domains composed of helices with the in-plane wavevector along the [100] axis (alternating red and green stripes), and possible helices with the out-of-plane wavevector along the [001] axis (dark areas). Further increasing the temperature above 300 K to approach T_C (about 325 K), the in-plane helices disappear and the dark area in Extended Data Fig. 1e (possible helices with the out-of-plane wavevector along the [001] axis) expands over the view area, revealing the planar magnetic anisotropy in the thin plate of Co₈Zn₉Mn₃. With the application of a normal field of 65 mT, a hex-SkL appears at 300 K (Extended Data Fig. 1f).

Simulations of magnetic configurations. In Extended Data Fig. 2, the distribution of the unit vector of the magnetic moment $n = (n_x, n_y, n_z)$ for Fresnel (defocused) TEM image simulation was prepared by approximating the magnetic configurations with the superposition of proper-screw-type helices as follows. For the square lattice, we (1) prepare two proper-screw helices with q vectors perpendicular to each other; (2) add each n component of the proper-screw helices; (3) add a uniform positive value n_z^{add} to the n_z component; and (4) normalize the length of the vectors at each site so that $|n| = (n_x^2 + n_y^2 + n_z^2)^{1/2} = 1$. Owing to step (3), core-up merons are selected and no core-down antimerons appear, as in Fig. 1e. For the hexagonal lattice, we (1) prepare three proper-screw helices q vectors at relative angles of $2\pi/3$ to each other; (2) add each n component of the proper-screw helices; and (3) normalize the length of the vectors at each site so that $|n| = (n_x^2 + n_y^2 + n_z^2)^{1/2} = 1$. **Fresnel image (defocused Lorentz TEM image) simulation.** We performed the Fresnel image (defocused Lorentz TEM) simulation for the magnetic configurations using a custom-made program. The magnetic phase shift was calculated using a Fourier approach³¹; parameters are listed in Extended Data Table 1.

We did not consider contributions to the electron phase from a stray magnetic induction field in the vacuum region. Although the parameters for the simulation, such as the dimensions of the magnetic configurations, the magnetization, the defocus length and the dynamic range of the images, are not exact and deviate from the experimental conditions, the resultant intensity distribution and magnetization maps are anticipated to be qualitatively correct.

It is hard to distinguish the sq-ML from the square skyrmion lattice using Fresnel images alone, because some different magnetic configurations can yield the same intensity distribution in Fresnel images. Therefore, the simulation alone cannot exclude the possibility of alternative magnetic configurations.

Various (meta)stable states realized by the processes in the temperature-magnetic-field plane in the thin plate of Co₈Zn₉Mn₃. Extended Data Fig. 3 shows the phase diagrams and several relevant Lorentz TEM images observed in the (001) thin plate of Co₈Zn₉Mn₃. In Extended Data Fig. 3a, the field cooling (FC) with $B = 60$ mT from above T_C to various temperatures below T_C followed by the increase in B results in the deformed hex-SkL at each temperature (red dashed lines). Similarly, after FC with $B = 60$ mT down to $T = 100$ K, then reducing (black arrow) B to 40 mT and subsequently raising the temperature (dashed blue line), we observe the deformed skyrmions robustly (Extended Data Figs 3c, d), but no sq-ML state. These results agree with previous experimental studies of metastabilized skyrmions in bulky and flaky chiral-lattice magnets^{25,26,32}.

The cases of 20-mT and 40-mT FC (Extended Data Fig. 3b) are different from that of 60-mT FC where the expansion of the hex-SkL phase was observed in the T - B plane. The 20-mT and 40-mT FC result in the appearance of the distinctive sq-ML phase (Extended Data Fig. 3e). However, as the magnitude of the cooling field is increased above 50 mT, the sq-ML is replaced by the hex-SkL. The sq-ML is also metastabilized with the 20-mT and 40-mT FC down to 150 K, but tends to collapse into the helical state with further decrease in T (for example, 100 K; Extended Data Fig. 3f). The helical state, once converted from the metastable sq-ML at lower temperature, always remains stable up to room temperature as long as B is less than 10 mT (see the low-field region along the abscissa in Extended Data Fig. 3b).

Various periodic arrays of the topological spin textures in the thin plate of Co₈Zn₉Mn₃. Various periodic arrays of topological spin textures, including the sq-ML at a lower field of 20-mT FC (Extended Data Fig. 4a–c), the hex-SkL at a field of 65-mT FC (Extended Data Fig. 4d–f) and skyrmion chains at a higher field of 180-mT FC (Extended Data Fig. 4g–i), are generated in a (001) thin plate of Co₈Zn₉Mn₃ at a temperature of 295 K. Lorentz TEM images (Extended Data Fig. 4a, d), the fast Fourier transforms (insets in Extended Data Fig. 4a, d) and related magnetization textures (Extended Data Fig. 4b, e) clearly represent the sq-ML with four-fold symmetry at the lower field and the hex-SkL with six-fold symmetry at the higher field, respectively. In addition to these lattice forms of topological spin textures, the curved skyrmion chains (Extended Data Fig. 4g, h) can be generated via a higher-field (180 mT) cooling procedure, indicating fertile topological states in the thin plate of Co₈Zn₉Mn₃. The magnified images of the topological spin textures (Extended Data Fig. 4c, f, i) reveal the differences in the topological number, shape and size between merons and skyrmions.

Changes in spontaneous magnetic structure in thin plates of Co-Zn-Mn with varying Mn composition. To characterize the in-plane magnetic anisotropy of the thin plates of Co-Zn-Mn with different T_C (T_C increases with decreases in the Mn composition), we performed a series of Lorentz TEM observations by varying the Mn compositions at zero field and 95 K, below the magnetic ordering temperature T_C . The electron-phase images (Extended Data Fig. 5i–l) were obtained by analysing defocused Lorentz TEM images (over-focused images shown in Extended Data Fig. 5a–d and under-focused images shown in Extended Data Fig. 5e–h) using the software Qpt. As described above, the in-plane magnetization can be evaluated from the phase shift according to equation (2). The white and dark contrasts with gradient in the electron-phase images are related to the in-plane magnetizations with opposite directions. In contrast to the ideal screw structure observed in Co₈Zn₈Mn₄ with a lower T_C of about 300 K, the band-shaped in-plane ferromagnetic domains (Extended Data Fig. 5l) appear in the CoZn thin plate with the higher T_C of about 460 K⁸. The decrease in Mn composition results in unbalanced domains with positive (white contrast) or negative (dark contrast) phase shift, showing that the magnetization stays longer in-plane compared with out-of-plane (compare Extended Data Fig. 5i and l). In other words, decreasing the Mn composition leads to the enhancement of in-plane magnetic anisotropy in Co-Zn-Mn thin plates^{18,33,34}.

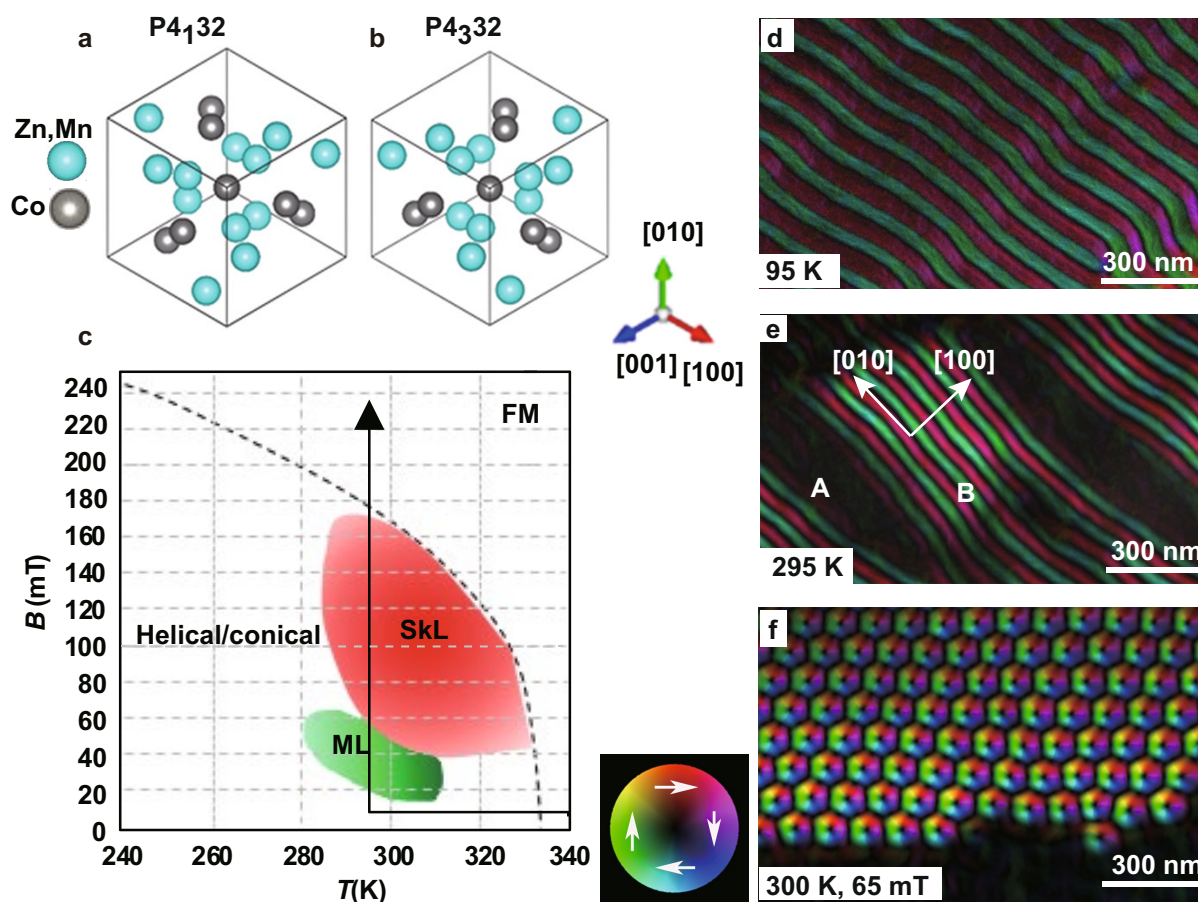
Exotic topological spin textures in thin plates of Co-Zn-Mn. We observed various exotic topological states (Extended Data Fig. 6) in the thin plates of Co-Zn-Mn with the application of magnetic fields normal to the plates. Extended Data Fig. 6a shows a Lorentz TEM image of skyrmion chains with a 90-mT field at room temperature in Co₈Zn₉Mn₃. Such unfavourable spin textures in chiral-lattice systems in terms of the Dzyaloshinskii–Moriya interaction may become plausible in thin films with in-plane magnetic anisotropy^{3,18}. With decreases in Mn composition, we observed the structure of two bound, deformed skyrmions of opposite helicity in

$\text{Co}_8\text{Zn}_{10}\text{Mn}_2$ (Extended Data Fig. 6b) and bubble-like domains in CoZn (Extended Data Fig. 6c), which points to the further enhancement of the in-plane anisotropy with a decrease in Mn composition in thin plates of Co-Zn-Mn.

Data availability

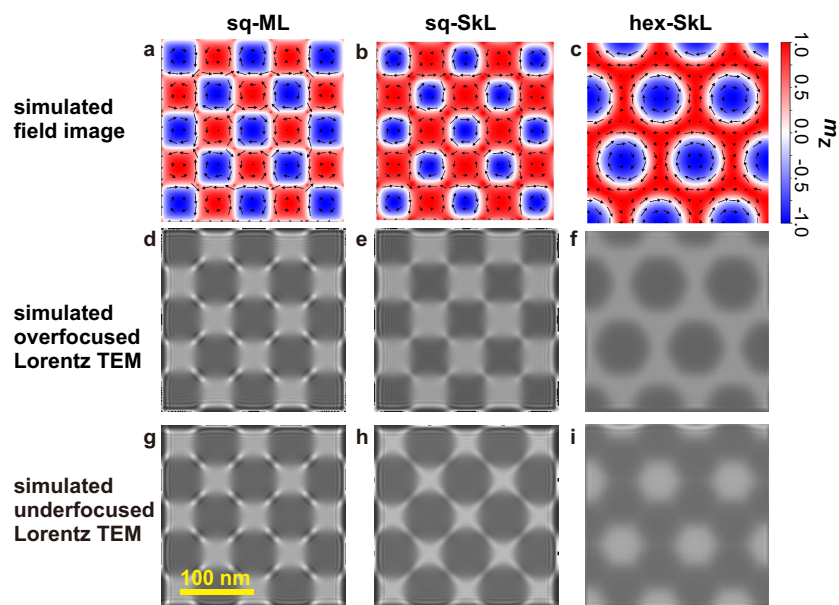
The data shown in the figures and that support the findings of this study are available from the corresponding author on reasonable request.

31. Beleggia, M. et al. Quantitative study of magnetic field distribution by electron holography and micromagnetic simulations. *Appl. Phys. Lett.* **83**, 1435 (2003).
32. Morikawa, D. et al. Deformation of topologically-protected supercooled skyrmions in a thin plate of chiral magnet $\text{Co}_8\text{Zn}_8\text{Mn}_4$. *Nano Lett.* **17**, 1637–1641 (2017).
33. Bogdanov, A. & Hubert, A. Thermodynamically stable magnetic vortex states in magnetic crystals. *J. Magn. Magn. Mater.* **138**, 255–269 (1994).
34. Hubert, A. & Schäfer, R. *Magnetic Domains* Chs. 2, 3 (Springer, Berlin, 1998).



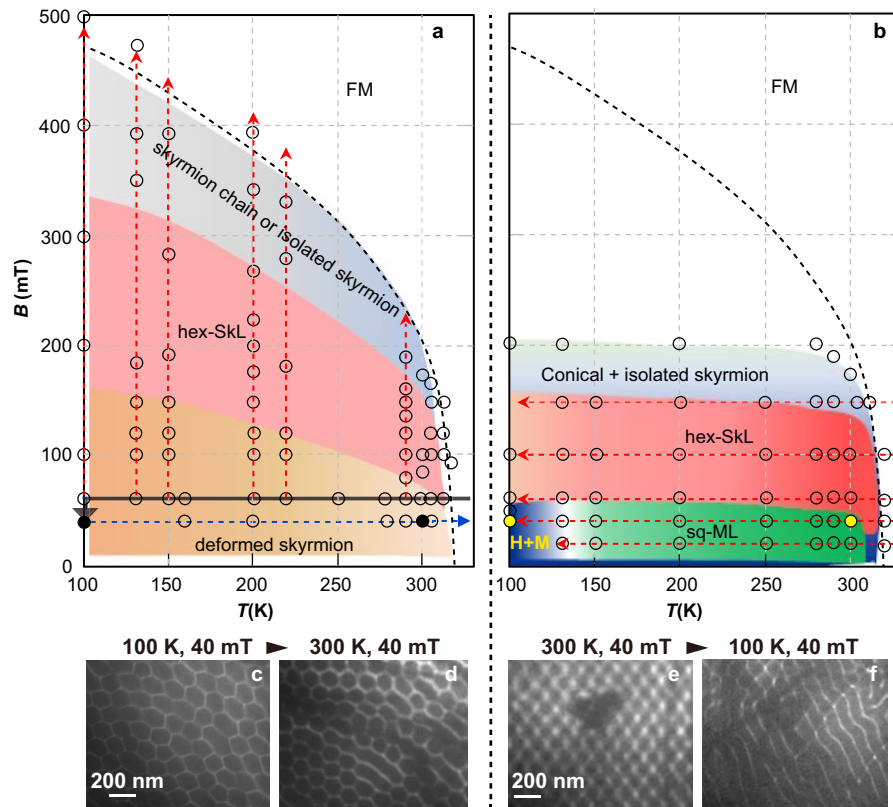
Extended Data Fig. 1 | The crystal structure, magnetic configurations and magnetic phase diagrams of the (001) thin plate of $\text{Co}_8\text{Zn}_9\text{Mn}_3$. **a, b**, Schematics of the crystal structure with space group $P4_132$ (**a**) and $P4_332$ (**b**). Coloured arrows indicate the crystal axes. **c**, Magnetic phase diagram (approximate) of the hex-SkL³⁰ and sq-ML observed over field-increasing runs from low (less than 10 mT) field cooling for a (001) thin plate of $\text{Co}_8\text{Zn}_9\text{Mn}_3$. The phase determination was based on the continuous magnetic-field scans at fixed temperatures in intervals of $\Delta T = 5$ K. The arrow indicates the field-increasing run for the Lorentz

TEM images shown in Fig. 2a–c. FM, field-magnetized ferromagnetic structure. **d, e**, Periodic stripe domains with a single wavevector along the [100] axis at 95 K (**d**), the helical structure with possible multi-domains composed of helices with in-plane wavevectors (area B) and with out-of-plane wavevectors (dark regions; area A) at 295 K (**e**), respectively. **f**, A hex-SkL realized under 65 mT at 300 K. Colours in **d–f** (see colour wheel) depict the direction (white arrows) of the local in-plane magnetization; black shows the out-of-plane magnetization.



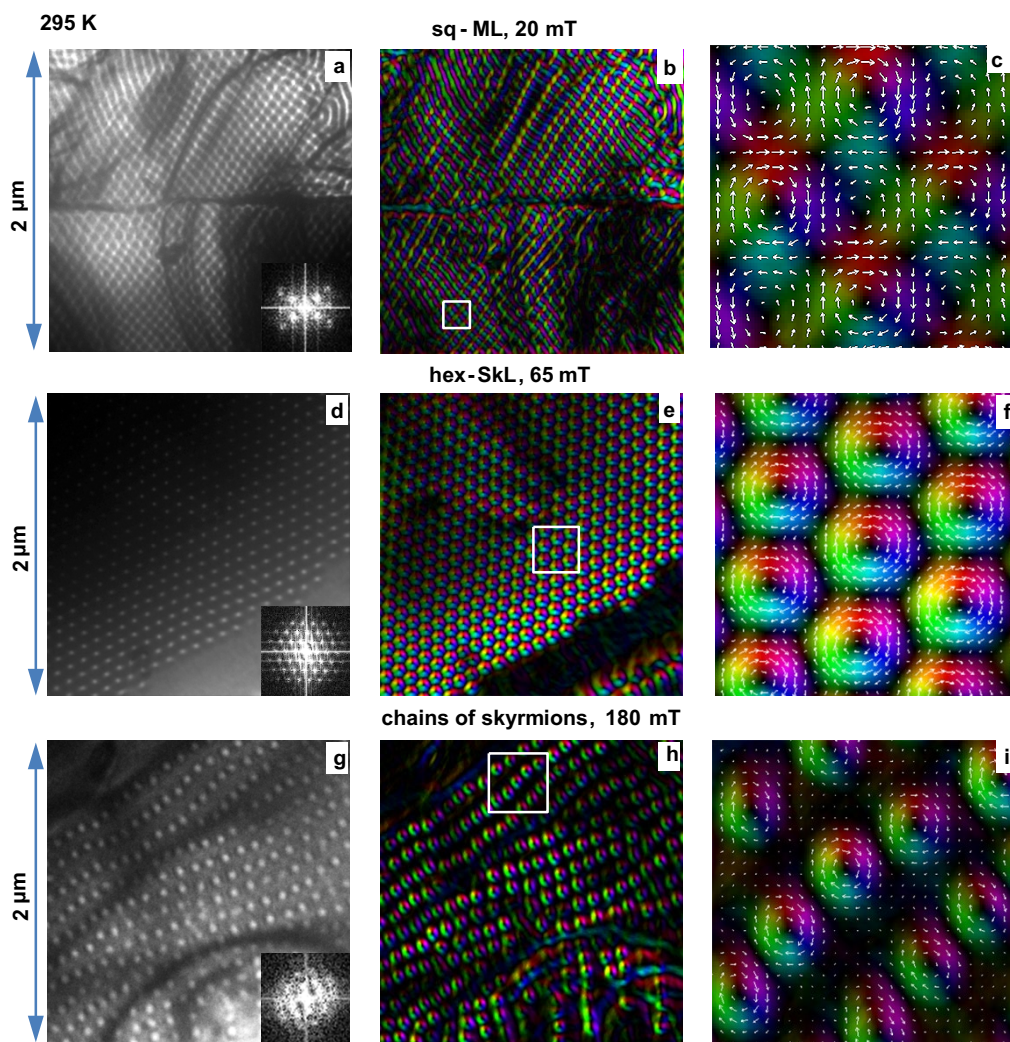
Extended Data Fig. 2 | The approximate in-plane magnetization textures and simulated defocused Lorentz TEM images. a, d, h, sq-ML. b, e, i, sq-SkL. c, f, j, hex-SkL. The parameters for the simulations are

shown in Extended Data Table 1. The colour bar indicates the normalized component of the out-of-plane magnetization m_z .



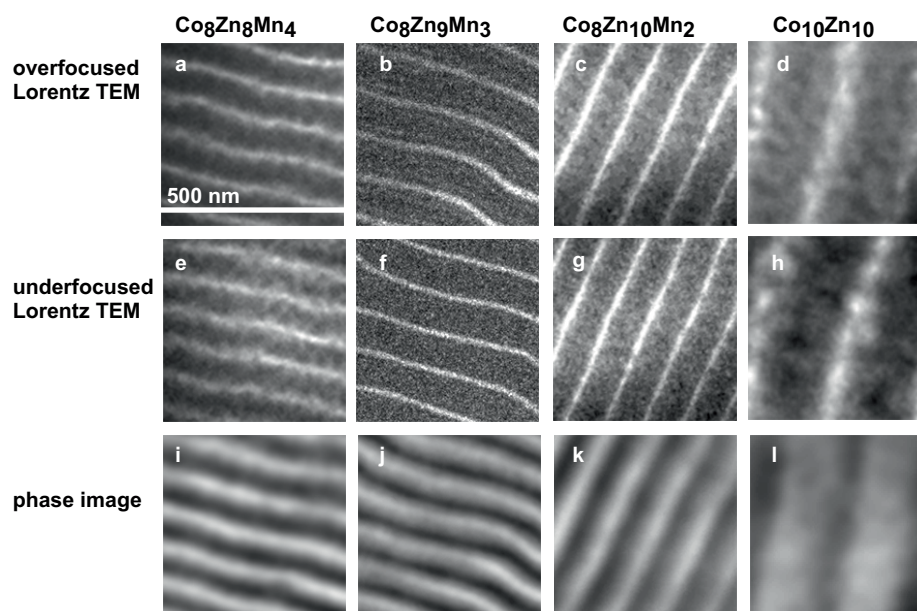
Extended Data Fig. 3 | Magnetic phase diagrams and several over-focused Lorentz TEM images observed in the (001) thin plate of $\text{Co}_5\text{Zn}_9\text{Mn}_3$ with varying temperature T and external magnetic field B . **a**, Phase diagram of the magnetic structure observed after 60-mT field cooling with increasing B (red dashed arrows), decreasing (black arrow) B and then increasing T (blue dashed arrow). **b**, Phase diagram of the magnetic structure observed after field cooling with various cooling fields

(indicated by red dashed arrows). H + M shows the mixed structure of helices (dominant) and merons (minor). The open circles specify the (T, B) points that we measured. The dark blue region shows the helical phase. **c–f**, Over-focused Lorentz TEM images observed for different T and B , indicated by black solid circles in **a** (**c**, **d**) and yellow solid circles in **b** (**e**, **f**).

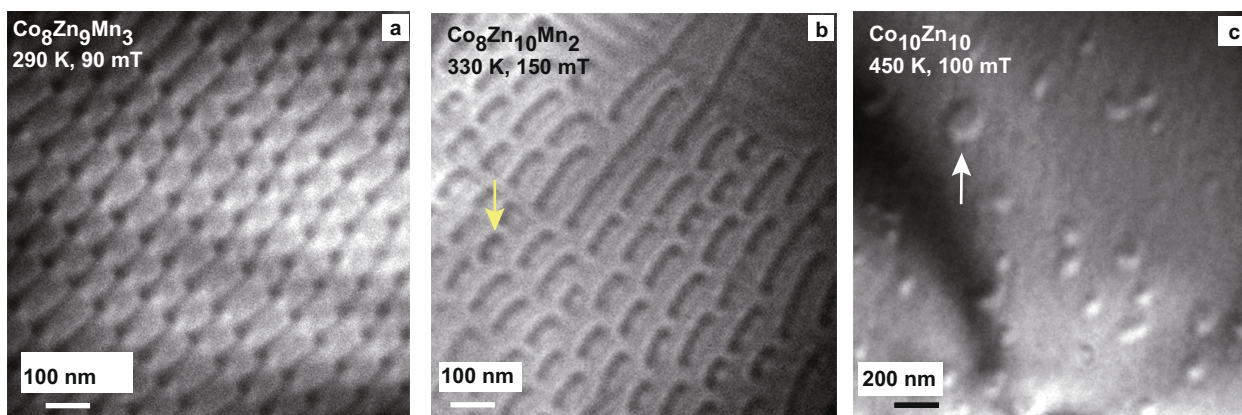


Extended Data Fig. 4 | Various periodic arrays of the topological spin textures observed in the (001) thin plate of $\text{Co}_8\text{Zn}_9\text{Mn}_3$ with varying external magnetic field. **a, b, d, e, g, h**, Lorentz TEM images (**a, d** and **g**; insets show the corresponding fast Fourier transforms) and their

magnetization maps (**b, e** and **h**) for the sq-ML (**a, b**), hex-SkL (**d, e**) and skyrmion chains (**g, h**) observed at 295 K and various fields. **c, f, i**, Magnified magnetization textures in the boxed areas in **b, e** and **h**.



Extended Data Fig 5 | Spontaneous magnetic structures in thin plates of Co-Zn-Mn with various Mn compositions. a–h, Defocused Lorentz TEM images observed in the thin plates of Co-Zn-Mn at zero field and 95 K. i–l, Electron-phase images obtained from analysing Lorentz TEM images in a–h with the transport-of-intensity equation.



Extended Data Fig. 6 | Exotic topological spin textures in thin plates of Co-Zn-Mn with various Mn compositions. a–c, Over-focused Lorentz TEM images of skyrmion chains observed in $\text{Co}_8\text{Zn}_9\text{Mn}_3$ (a), bound

skyrmions in $\text{Co}_8\text{Zn}_{10}\text{Mn}_2$ (b; such as that indicated by the yellow arrow) and bubble-like domains in $\text{Co}_{10}\text{Zn}_{10}$ (c; such as that indicated by the white arrow).

Extended Data Table 1 | Parameters for Fresnel image simulations

Parameter	Value
M (at 300 K)	$5.7\mu_B/\text{f.u.}$
v	0.26 nm^3
B	$\mu_0 M/v = 0.26\text{ T}$
t	100 nm
V_{acc}	200 kV
C_s	1 mm
Δf	$30\text{ }\mu\text{m}$

M , μ_B , μ_0 , v , B , t , V_{acc} , C_s and Δf denote the local magnetic moment per formula unit, Bohr magneton, vacuum permeability, the unit-cell volume of the crystal lattice, the magnetic induction, the sample thickness, the accelerating voltage of the microscope, the spherical aberration of the microscope and the defocus depth of the Fresnel image in Lorentz TEM mode, respectively.